Chemical Science

ROYAL SOCIETY OF CHEMISTRY

EDGE ARTICLE

View Article Online
View Journal | View Issue

Cite this: *Chem. Sci.*, 2025, **16**, 2420

All publication charges for this article have been paid for by the Royal Society of Chemistry

Exploring the diffusion of DNA strands into nanoporous structures for establishing a universal electrochemical biosensor†

Cong-Lin Zhao,[a] Runlei Gao,[a] Yinzheng Niu,[a] Bin Cai *[ab] and Ye Zhu *[ab]

Received 30th August 2024
Accepted 30th December 2024

DOI: 10.1039/d4sc05833j

rsc.li/chemical-science

The development of universal electrochemical sensing platforms with high sensitivity and specificity is of great significance for advancing practical disease diagnostic methods and devices. Exploring the structural properties of electrode materials and their interaction with biomolecules is essential to developing novel and distinctive analytical approaches. Here, we innovatively investigated the effect of DNA length and configuration on DNA molecule transfer into the nanostructure of a nanoporous gold (NPG) electrode. The NPG electrode can not only distinguish and quantify short DNA strands but can also prevent the diffusion of long DNA, thereby minimizing or eliminating background interference. Leveraging these findings, we developed a universal DNA-based NPG electrochemical biosensing platform for the detection of different types of biomolecules. As a proof-of-concept, this sensing platform was integrated with nuclease-assisted target-recycling recognition and amplification reactions to achieve sensitive and specific detection of single-stranded DNA, microRNA-21, and carcinoembryonic antigen, with detection limits of 4.09, 27.4, and 0.28 fM, respectively. The demonstrated universality, sensitivity, specificity, and capability for analyzing complex samples ensure a comprehensive and robust detection approach for nucleic acid-based molecular diagnosis.

Introduction

Biomarkers, such as small molecules, proteins, nucleic acids, and cells, are usually quantitated as indicators for disease diagnosis and individualized therapy because of their involvement in physiological or pathological processes.[1–3] Among approved biomarkers, proteins and nucleic acids account for more than 90% of the total.[4] Their reliable determination is of great significance for clinical applications. In addition to commercialized techniques like enzyme-linked immunosorbent assay (ELISA) for protein analysis and polymerase chain reaction (PCR) for nucleic acid analysis, significant efforts have been directed toward developing novel sensing approaches with enhanced performance in various aspects.[5–8] However, most methods are limited to detecting specific analytes or a single category of analytes. Advanced research has revealed that the development and prognosis of some diseases involve multiple complex molecular events, and some biomarkers are shared across different diseases.[9,10] Therefore, quantitating a single biomarker is often insufficient for reliable disease diagnosis. There is an urgent need to develop universal sensing approaches with high sensitivity for the detection of different categories of biomarkers.[11–14]

The implementation of every biosensing principle relies on detection reagents for analyte recognition and signalling, and sensing platforms for signal transduction. Undoubtedly, a simple and universal sensing platform is significant for both manufacturers and users, especially in point-of-care applications. Among commonly employed signal transduction techniques, electrochemical sensing platforms are widely recognized as promising candidates for point-of-care diagnostic devices due to their simplicity, rapid response, low cost, miniaturization, and multiplexing capabilities through seamless integration with signal processing electronics.[15–18] Electrodes, as vital components of electrochemical sensors, significantly influence sensor performances.[19,20] The employment of advanced electrode materials has greatly improved the overall performance of electrochemical sensors. For instance, nanoporous electrode materials, due to their structural advantages, have enhanced sensor sensitivities, anti-biofouling properties,

[a]*School of Chemistry and Chemical Engineering, Shandong University, Jinan 250100, China. E-mail: bin.cai@sdu.edu.cn; zhuye@sdu.edu.cn*

[b]*Shenzhen Research Institute of Shandong University, Shenzhen 518000, China*

† Electronic supplementary information (ESI) available: Experimental procedures, characterization results of NPG and NPG/AuE, electrochemical behaviour of free MB on AuE and NPG/AuE, the electrochemical response variation of AuE over time towards MB-labelled ssDNA with different number of bases, the maximum signal response variation of AuE and NPG/AuE towards MB-labelled ssDNA with different number of bases, the signal response of AuE and NPG/AuE towards different concentrations of ssDNA(5)-MB, the calibration plots of Exo III, csDNA, miRNA-21, and CEA on AuE and NPG/AuE, selectivity of the proposed strategy, the calibration plots of Exo III, csDNA, miRNA-21, and CEA in spiked serum samples, sequence information of the nucleic acids used in this work, and comparison of this strategy with other methods. See DOI: https://doi.org/10.1039/d4sc05833j

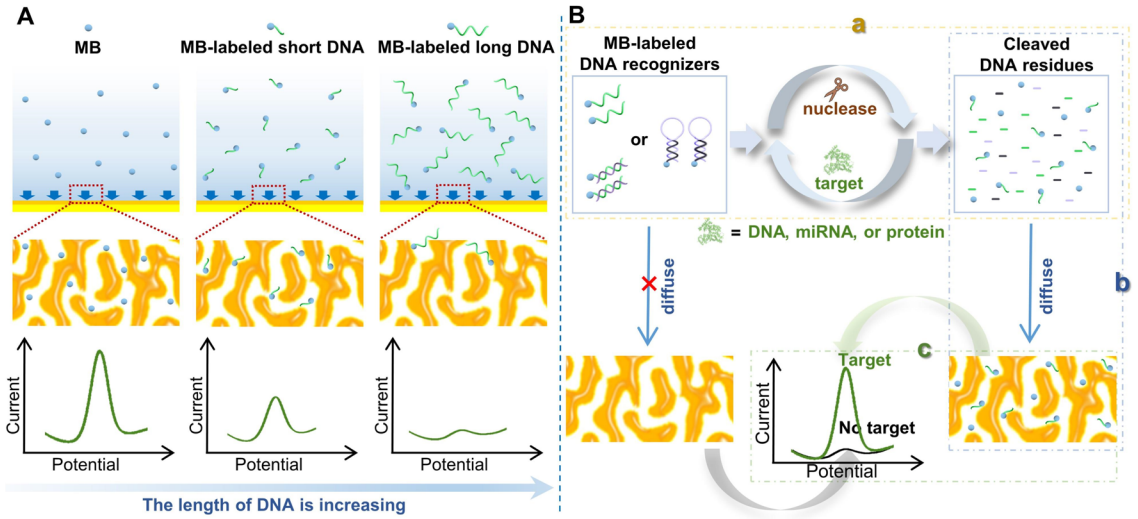

Scheme 1 (A) Illustration of the response current variation with DNA length on the NPG sensing platform. (B) Schematic diagram of the working principle of the DNA-based NPG electrochemical biosensor for the universal detection of DNA, miRNA, and protein, which is composed of three modules: (a) nuclease-assisted target-recycling recognition and amplification module, (b) NPG platform-based signal molecule enrichment module, and (c) signal conversion module.

and mass transfer abilities.[21–24] Recently, nucleic acid-based electrochemical biosensors have attracted extensive attention. Their unique properties like broad recognition capability for different categories of targets, powerful signal amplification ability through various nuclease-assisted reactions, and easy chemical synthesis and modification make nucleic acids, particularly DNA, highly suitable for the development of electrochemical biosensors.[25–28] Seker and co-workers have systematically explored the influence of nanoporous gold (NPG) morphology on DNA hybridization efficiency and electrochemical DNA sensor performance by using a DNA sequence with a constant length.[29,30] However, the similar relationship with the parameters of DNA as variates has rarely been studied. It is well known that DNA is a special class of biomolecules with adjustable length, composition, and configuration, as well as unique programmability. Especially in nuclease-assisted reactions, the length and configuration of DNA sequences may change as the reaction progresses. It can be inferred that DNA sequences with varied length or configuration will exhibit differentiated mass transfer performance because of geometric accessibility. In this regard, it is worthwhile to reveal the effect of DNA length and configuration on DNA molecule transfer into the nanostructure of porous electrodes, which is crucial for reasonable design of sensitive, accurate, comprehensive, robust, yet simple and cost-effective DNA-based electrochemical sensors.

For this purpose, an NPG electrochemical sensing platform was developed to investigate the transfer behavior of DNA sequences with varied lengths and configurations. Each DNA sequence was tagged with methylene blue (MB) for electrochemical signal transduction to systematically study the structure–property relationship between the DNA length/configuration and the corresponding electrochemical response. Interestingly, the obtained response current observably decreases with the increasing DNA base number, even one-base difference (Scheme 1A). Based on this finding, a universal sensing strategy was proposed for the detection of different categories of targets, such as DNAs, microRNAs (miRNAs), and proteins. As illustrated in Scheme 1B, the proposed sensing strategy could be divided into three modules, (a) nuclease-assisted target-recycling recognition and amplification module, (b) NPG platform-based signal molecule enrichment module, and (c) signal conversion module. For different categories of targets, only the first module is different in reagents and related reaction conditions, while the other two modules are exactly the same. The universality of the proposed sensing principle and the developed NPG-based sensing platform was verified by specific detection of exonuclease III (Exo III), single-stranded DNA, miRNA-21, and carcino-embryonic antigen (CEA), demonstrating significant promise for the development of comprehensive and robust point-of-care systems for the healthcare industry.

Results and discussion

Characterization of the NPG/AuE platform

The NPG film was firstly characterized by SEM and TEM. As shown in Fig. S1,† the obtained NPG film exhibits a typical three-dimensional bicontinuous nanoporous structure, which is expected to provide an accessible passage for mass transfer. The pore width is observed to be similar to the ligament width. Most of the pore width distributes in the range of 15–40 nm, with an average value around 25.5 nm. The standard deviation of the average pore width among different batches of NPG is as low as 0.0365, indicating remarkable uniformity and reproducibility of the prepared NPG. The modification of a gold electrode (AuE) with NPG film was characterized by electrochemical impedance spectroscopy (EIS) in 0.1 M KCl solution

containing 5.0 mM $[Fe(CN)_6]^{3-/4-}$ (Fig. S2†). A Nyquist diagram with a small semicircle is obtained for the bare AuE, and the R_{ct} value is fitted to be about 152.4 Ω. After attachment of NPG, a smaller semicircle is observed and the fitted R_{ct} value drops to 20.11 Ω, indicating the improvement of the electrode conductivity by NPG. EIS characterization confirms the successful construction of the NPG/AuE sensing platform. Furthermore, the NPG/AuE sensing platform was evaluated by cyclic voltammetry in 0.5 M sulfuric acid between −0.2 V and 1.6 V (Fig. S3†). The obtained cyclic voltammograms of different batches of NPG/AuE platforms are almost overlapped completely, suggesting excellent batch-to-batch reproducibility of the effective sensing surface area. Compared with planar AuE, the characteristic redox peak of NPG/AuE increases sharply. Based on the electrical charge involved in the gold oxide reduction peak,[31] the effective surface area of NPG/AuE is calculated to be 0.49 cm^2. Compared with the planar AuE, the roughness of NPG/AuE is calculated to be 3.14, indicating that NPG has a great enlargement effect on the effective electrode surface area.

Electrochemical behavior of free MB

To establish a better understanding of the diffusion of DNA molecules into the NPG film, the electrochemical behavior of free MB molecules, which serve as an electrochemical indictor of DNA sequences, was studied in advance. Upon the immersion of NPG/AuE into the Tris–HCl buffer solution containing 1 μM MB, a typical oxidation peak related with MB is observed around −0.25 V in the differential pulse voltammetry (DPV) response (Fig. S4†). In contrast, almost no response is observed on the AuE in the same solution, demonstrating the superior sensing performance of NPG that is ascribed to its unique nanoporous structure and excellent electrochemical catalytic properties.[32]

Subsequently, the diffusion behavior of MB into the nanoporous structure of NPG/AuE was carefully studied by recording the DPV response of MB over time, with bare AuE as a control. As shown in Fig. S5,† the response current on the bare AuE gradually increases with the increasing immersion time in the first half and reaches a plateau after 2.5 h, suggesting the adsorption equilibrium of MB molecules onto the planar AuE surface. The corresponding data fitting displays a pseudo-first-order kinetic model, with a fitting equation of I_p (μA) = $0.2875 \times (1 - e^{-1.3165t})$ and a correlation coefficient of 0.992. Interestingly, a different phenomenon is observed for the NPG/AuE (Fig. S6†), on which the response current continuously increases throughout the whole test process of 30 h, indicating unimpeded mass transfer of MB in the nanoporous structure of NPG/AuE. Moreover, the constantly enlarged electrode–electrolyte interface vastly strengthens the response current on the NPG/AuE. At 2.5 h, when the response current on the bare AuE reaches a plateau, the response current on the NPG/AuE is approximately 15 times higher than that on the bare AuE, implying the great potential of NPG in serving as a highly sensitive sensing platform. According to the trend of the current–time plot on NPG, the whole diffusion process could be divided into two sections, the liquid film diffusion process and intra-pore diffusion process. The current–time relationship for each section is fitted to obey the linear equation of I_p (μA) = $1.6529t + 0.3207$ and I_p (μA) = $0.3756t + 3.7578$, respectively. By comparison, the MB diffusion rate in the liquid film is faster than that in the pores, which is in line with the rules of the pore diffusion model. These results provide a basis for the exploration of DNA diffusion into the NPG nanoporous structure.

Electrochemical study on the diffusion behaviour of DNA with varied length or configuration

An electrochemical study on the diffusion behavior of DNA sequences with varied lengths or configurations was conducted based on the electrochemical response of the MB tag that was labelled on each DNA terminal. The detailed sequence information is listed in Table S1.† The straight single-stranded DNA (ssDNA) sequences containing 5, 6, 8, 10, and 22 bases were denoted as ssDNA(5)-MB, ssDNA(6)-MB, ssDNA(8)-MB, ssDNA(10)-MB, and ssDNA(22)-MB, respectively. As the AuE is immersed into the Tris–HCl buffer solution containing 1 μM different ssDNA molecules, all the response currents gradually increase with increasing time in the first half (Fig. S7†), implying the approaching process of the DNA molecules towards the electrode surface. These response currents reach the maximum value in around 60 min, and then begin to decline, which might be owing to the adsorption equilibrium of the MB-labelled ssDNA molecules on the electrode surface and the consumption of the labelled MB by the unidirectional DPV scanning. Interestingly, the longer the DNA strand is, the smaller the obtained maximum response signal value is, indicating that a smaller amount of longer DNA molecules reaches the AuE surface because of the steric effect. In general, there is no significant difference in the current response toward varied DNA lengths (Fig. S8†). By contrast, the NPG/AuE exhibits very different current response variation toward ssDNA molecules with different lengths (Fig. 1A). The response current dramatically increases with the immersion time, and then reaches a plateau within 30 min, without a decline in the prolonged immersion time, suggesting the remarkable superiority of NPG in mass transfer. It is worth noting that the fewer bases the DNA strand contains, the shorter the time needed to reach

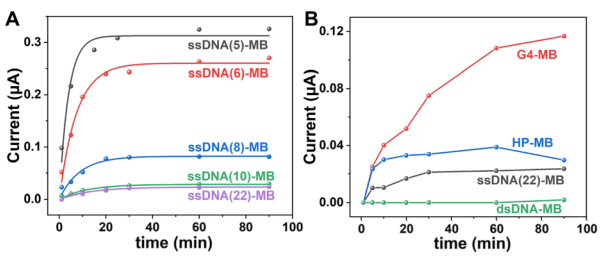

Fig. 1 (A) The DPV response current of NPG/AuE over time in Tris–HCl buffer solution containing 1 μM ssDNA(5)-MB, ssDNA(6)-MB, ssDNA(8)-MB, ssDNA(10)-MB, and ssDNA(22)-MB, respectively. (B) The DPV response current of NPG/AuE over time in Tris–HCl buffer solution containing 1 μM DNA with different configurations, ssDNA(22)-MB, G4-MB, HP-MB, and dsDNA-MB.

equilibrium and the higher the achieved maximum response current value is. Most importantly, the NPG/AuE sensing platform could effectively identify the short-stranded DNA containing varied bases, even one-base differences (Fig. S8†). On the other hand, this platform can effectively prevent long-stranded DNA with more than 10 bases from reaching the electrode surface and result in almost negligible electrochemical signals, revealing inherent discrimination in DNA length. The mechanism behind these findings is based on the geometric effect-dependent sieving function of the nanoporous structure of NPG, which is similar to Seker's findings[29,30] to some extent. Furthermore, the response current of the NPG/AuE sensing platform toward different DNA strands is analyzed and fitted over time (Fig. 1A). It conforms to the pseudo-first-order dynamics model, and the fitting equation is I_p (μA) = $i_{eq}(1 - e^{-kt})$, where i_{eq} is the current value at diffusion equilibrium and k is the diffusion rate constant. The specific data for each MB-labelled DNA strand is shown in Table S2.† With the growth of DNA length, both the diffusion rate and the current value at diffusion equilibrium decrease gradually. These obtained results suggest that the fabricated NPG/AuE sensing platform can be used to distinguish and quantify the short-stranded DNAs, while excluding the interference of long DNA strands by preventing their diffusion to the electrode surface.

Considering the adjustable secondary structure of DNA, which might impact its movement, the effect of DNA configuration on its diffusion behavior was also studied in addition to DNA length, including straight ssDNA(22)-MB, hairpin structure DNA (HP-MB) containing 22 bases, guanine-quadruplex DNA (G4-MB) containing 22 bases, and double-stranded DNA (dsDNA-MB) that was formed by ssDNA(22)-MB and its complementary sequence (csDNA). Obviously, the DNAs with different configurations display different signal responses (Fig. 1B). Compared with ssDNA(22)-MB, G4-MB and HP-MB exhibit enhanced response, which might be ascribed to the formation of a rigid G-quadruplex or hairpin structure that clearly reduces the apparent size of DNA and facilitates the mass transfer into the porous structure of NPG. In particular, G4-MB shows the highest response current because of its compact structure. In contrast, dsDNA-MB, which has a similar maximal length to ssDNA(22)-MB, exhibits significantly reduced response current due to its rigid structure. The different response associated with the DNA length and configuration inspires us to develop a highly sensitive electrochemical sensing approach with low background by adjusting the DNA composition and configuration.

Relationship between signal and DNA concentration

The above results have successfully demonstrated the qualitative analytical performance of the developed NPG/AuE sensing platform in distinguishing DNA strands with varied length and configuration. Furthermore, it is necessary to investigate its quantitative analytical performance, which is critical for the development of a general-purpose sensing approach. For this purpose, ssDNA(5)-MB at varied concentrations was detected by the developed NPG/AuE sensing platform as a model. As shown in Fig. S9A,† the DPV response signal gradually increases with the increasing concentration of ssDNA(5)-MB. A good linear relationship between the current response and the ssDNA(5)-MB concentration is obtained in the range of 0.4–1 μM, with a linear correlation equation of I_p (μA) = $0.5273c_{ssDNA(5)\text{-}MB}$ (μM) − 0.2011 and a correlation coefficient of 0.998 (Fig. S9B†). The detection limit is calculated to be 147.6 nM ssDNA(5)-MB (defined as S/N = 3). This demonstrates the excellent quantitative analytical performance of the NPG/AuE sensing platform and lays the foundation for the subsequent development of general-purpose sensors. In addition, control experiments using AuE as a substitute for NPG/AuE were conducted (Fig. S9B†). Although there is also a linear relationship between the response current and the ssDNA(5)-MB concentration, the sensitivity, linear correlation, and stability are not as good as for the NPG/AuE sensing platform, suggesting that NPG enables effective enrichment of the MB-labelled short DNA chain, rather than simple random adsorption on the planar electrode.

Universality of the NPG-based sensing platform

Based on the findings obtained from the study on the diffusion behavior of DNA, we combined the developed NPG/AuE sensing platform with nuclease-assisted target recycling recognition and amplification reactions for sensitive detection of various targets (Scheme 1B). In the absence of specific targets, the designed recognizers will be prevented from diffusing into the nanostructure of NPG because of their large geometric size. In contrast, the presence of a specific target will lead to the conformational switching of the MB-tagged DNA recognizers and trigger the specific cleavage of the recognizers by the corresponding nuclease, followed by the generation of short MB-tagged DNA residues and recycling of the target. Compared with the intact recognizers, the short MB-tagged DNA residues can easily diffuse into the nanostructure of NPG and transduce the redox reaction of MB into detectable signals. Hence, various analytical purposes involving DNA reactions can be achieved through reasonable and ingenious design.

To explore the universal analytical performance of the NPG/AuE sensing platform, nuclease activity was evaluated first by detecting Exo III as a model. As displayed in Fig. 2A, upon the addition of Exo III into the Tris–HCl buffer solution containing abundant dsDNA-MB, which is formed by fully complementary ssDNA(22)-MB and csDNA, the ssDNA(22)-MB in the dsDNA-MB is hydrolyzed by Exo III from the blunt 3′ end, leaving the released MB tag. According to the response difference of the NPG/AuE sensing platform towards DNA with varied length and configuration, the released MB can easily diffuse into the pore structure of the NPG/AuE sensing platform and generate a clear detection signal, while the intact dsDNA-MB is intercepted due to the steric effect and gives insignificant signal. Therefore, the obtained sensor response can be utilized to evaluate the activity of Exo III. The recorded DPV responses of the NPG/AuE sensing platform towards different concentrations of Exo III are displayed in Fig. 2B, where the peak current gradually increases with the increasing Exo III concentration. The corresponding calibration curve exhibits a good linearity from 0.0001 U μL^{-1} to

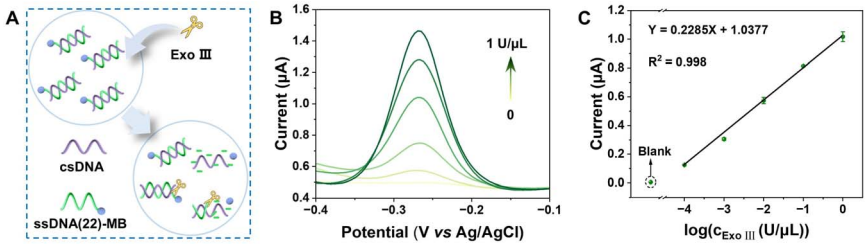

Fig. 2 (A) Schematic diagram of the sensitive detection of Exo III. (B) The DPV response of the NPG/AuE sensing platform towards different concentrations of Exo III (0, 0.0001, 0.001, 0.01, 0.1, and 1 U μL^{-1}, respectively). (C) The corresponding linear relationship between response current and the logarithm of Exo III concentration.

1 U μL^{-1} Exo III (Fig. 2C). The linear dependencies of Exo III analysis yields an equation, I_p (μA) = 0.2285 log($c_{Exo\ III}$ (U μL^{-1})) + 1.0377, with a correlation coefficient of 0.998. The detection limit of Exo III is calculated to be 0.045 U mL^{-1}, which is comparable with previous reports.[33,34]

The analytical performance of the NPG/AuE sensing platform for DNA detection was evaluated by using csDNA as a model target. As illustrated in Fig. 3A, csDNA can be recognized by ssDNA(22)-MB to form dsDNA-MB. The ssDNA(22)-MB strand in the dsDNA-MB duplex, with a blunt 3′-terminus, can induce the hydrolysis of Exo III. In contrast, the csDNA in the dsDNA-MB duplex cannot be hydrolyzed because of phosphorothioate modification of its 3′-terminus. In the practical analytical applications, the hydrolysis of the targets also could be prevented because of the protruding 3′-terminus. Thus, the intact csDNA is released after the hydrolysis of ssDNA(22)-MB and shift into the next recognition cycle. Finally, the released MB tag from the hydrolysis of ssDNA(22)-MB can diffuse into the porous structure of the NPG/AuE sensing platform for signal transduction. The designed sensing strategy was first verified with 12% polyacrylamide gel electrophoresis (PAGE) analysis (Fig. 3B). Lane a and lane b exhibit the bands for ssDNA(22) and csDNA, respectively. The recognition of csDNA by ssDNA(22) results in a slower band representing the formed dsDNA duplex in lane c. The lower band in lane c is associated with the unbound ssDNA(22), whose concentration is double that of csDNA. With the addition of Exo III into the mixture of ssDNA(22) and csDNA, a single band is observed (lane e), which appears at a similar position to csDNA in lane b, indicating the specific hydrolysis of the formed dsDNA duplex by Exo III and the resulting release-recycling of the intact csDNA. Otherwise, ssDNA(22) could not be hydrolyzed by Exo III in the absence of the target csDNA (lane d). Then, the developed NPG/AuE sensing platform was used to detect csDNA with varied concentrations from 10 fM to 100 nM in Tris–HCl buffer. As shown in Fig. 3C, the recorded DPV curves display gradually enhanced peak current as the csDNA concentration increases. A good linearity between the response current and the logarithm of csDNA concentration is observed (Fig. 3D). The linear regression equation is I_p (μA) = 0.0908 log(c_{csDNA} (M)) + 1.6445, with a correlation coefficient of 0.994. The detection limit is as low as 4.09 fM, exhibiting good sensitivity compared with the previous reports.[35–37]

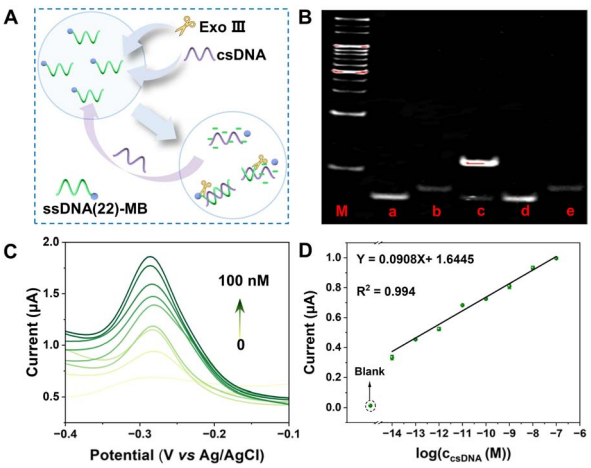

Fig. 3 (A) Schematic diagram of the sensitive detection of csDNA. (B) PAGE verification of the csDNA detection principle: (M) DNA marker (20, 40, 60, 80, 100, 120, 140, 160, 180, 200, 300, 400, 500 bp), (a) ssDNA(22), (b) csDNA, (c) ssDNA(22) + csDNA, (d) ssDNA(22) + Exo III, (e) ssDNA(22) + csDNA + Exo III. The concentration of ssDNA(22), csDNA, and Exo III are 1 μM, 0.5 μM, and 1 U μL^{-1}, respectively. (C) The DPV response of the NPG/AuE sensing platform towards different concentrations of csDNA (0, 10 fM, 100 fM, 1 pM, 10 pM, 100 pM, 1 nM, 10 nM and 100 nM, respectively). (D) The linear relationship between response current and the logarithm of csDNA concentration.

Next, the analytical ability of the NPG/AuE sensing platform for miRNA was investigated by detecting miRNA-21 as a model. The detection principle is shown in Fig. 4A. ssDNA(22)-MB, which is designed perfectly complementary to miRNA-21, serves as the recognizer and the signal reserve. In the presence of miRNA-21, it is recognized by ssDNA(22)-MB to form a DNA/RNA duplex. In this case, double specific nuclease (DSN), which possesses strong preference for cleaving the double-stranded DNA with more than 10 bp or the DNA strand in a DNA/RNA perfect duplex with more than 15 bp, is utilized to realize the recycling of target miRNA-21 by hydrolyzing the hybridized ssDNA(22)-MB. As a result, small MB tags are continuously released and easily reach the NPG/AuE sensing platform to generate an electrochemical signal. In contrast, it is difficult for the intact ssDNA(22)-MB sequence to reach the NPG/AuE sensing platform without the participation of miRNA-21 and DSN. The PAGE experiment demonstrated the successful recognition of miRNA-21 by ssDNA(22) and the formation of the

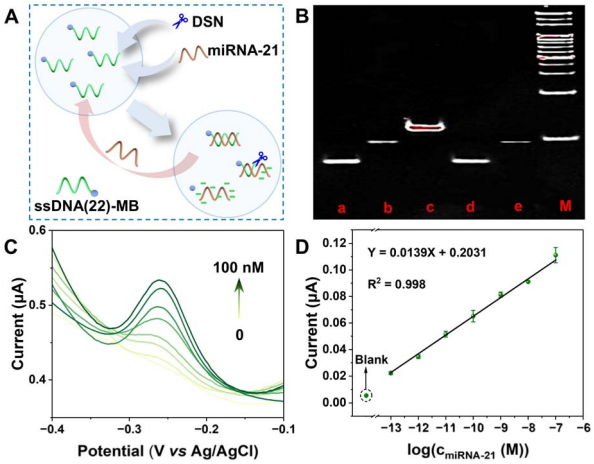

Fig. 4 (A) Schematic diagram of the sensitive detection of miRNA-21. (B) PAGE verification of the miRNA-21 detection principle: (a) ssDNA(22), (b) miRNA-21, (c) ssDNA(22) + miRNA-21, (d) ssDNA(22) + DSN, (e) ssDNA(22) + miRNA-21 + DSN, (M) DNA marker (20, 40, 60, 80, 100, 120, 140, 160, 180, 200, 300, 400, 500 bp). The concentrations of ssDNA(22), miRNA-21, and DSN are 1 μM, 1 μM, and 0.005 U μL^{-1}. (C) The DPV response of the NPG/AuE sensing platform towards different concentrations of miRNA-21 (0, 100 fM, 1 pM, 10 pM, 100 pM, 1 nM, 10 nM, and 100 nM, respectively). (D) The linear relationship between response current and the logarithm of miRNA-21 concentration.

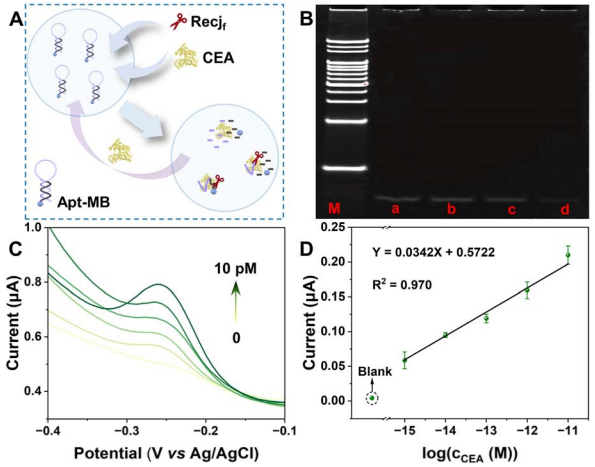

Fig. 5 (A) Schematic diagram of the sensitive detection of CEA. (B) PAGE verification of the CEA detection principle: (M) DNA marker (20, 40, 60, 80, 100, 120, 140, 160, 180, 200, 300, 400, 500 bp), (a) Apt, (b) Apt + CEA, (c) Apt + $RecJ_f$, (d) Apt + CEA + $RecJ_f$. The concentrations of Apt, CEA, and $RecJ_f$. are 200 nM, 100 nM, and 0.005 U μL^{-1}, respectively. (C) The DPV response of the NPG/AuE sensing platform towards different concentrations of CEA (0, 1 fM, 10 fM, 100 fM, 1 pM, and 10 pM, respectively). (D) The linear relationship between response current and the logarithm of CEA concentration.

RNA/DNA duplex (lane a–c in Fig. 4B). In the presence of DSN, the RNA/DNA duplex is destroyed through the hydrolysis of ssDNA(22), releasing intact miRNA-21 (lane e). To verify the specificity of DSN and avoid a false-positive signal, a control experiment without miRNA-21 was conducted. As displayed in lane d, the mixture of ssDNA(22) and DSN reveals an identical band with lane a only containing ssDNA(22), indicating the high specificity of the designed sensing strategy. The above PAGE experiment results preliminarily demonstrate the feasibility of the designed sensing strategy for miRNA-21. Afterwards, varied concentrations of miRNA-21 were determined based on the NPG/AuE sensing platform. As shown in Fig. 4C, the obtained DPV signal gradually increases with the increasing miRNA-21 concentration. The corresponding calibration curve exhibits a good linearity in the range of 100 fM to 100 nM miRNA-21, with a fitting equation of I_p (μA) = 0.0139 log($c_{miRNA\text{-}21}$ (M)) + 0.2031 and a correlation coefficient of 0.998 (Fig. 4D). The detection limit is determined to be 27.4 fM miRNA-21, which is comparable with previous reports.[38–40]

Furthermore, the analytical ability of the NPG/AuE sensing platform for proteins was explored by detecting CEA as a model. As shown in Fig. 5A, the aptamer for CEA (in purple) is sealed in a hairpin structure, which is designed with a MB-labelled flush 5′ terminal and denoted by Apt-MB. In the presence of CEA, the sealed aptamer segment recognizes and binds to CEA, resulting in unfolding of Apt-MB. In this case, $RecJ_f$ exonuclease ($RecJ_f$), which can catalyze the stepwise removal of nucleotides from single-stranded DNA in the 5′ to 3′ direction, is utilized to realize the recycling of target CEA by hydrolyzing the Apt-MB. Meanwhile, MB tag is continuously released and diffuses into the porous structure of the NPG/AuE sensing platform for signal transduction. The feasibility of the detection strategy was verified by PAGE experiment (Fig. 5B). The band in lane a corresponds to Apt. Because the CEA concentration is only half of the Apt concentration, the mixture of Apt and CEA in lane b still exhibits the band corresponding to Apt. When $RecJ_f$ is added into the mixture, however, no obvious band appears (lane d), indicating the successful hydrolysis of the unfolded Apt by $RecJ_f$ and the recycling of the CEA. In the absence of CEA, the mixture of Apt and $RecJ_f$ in lane c displays a similar band with that in lane a, suggesting that Apt can not be hydrolyzed by $RecJ_f$ without CEA and the false positive signal can be avoided. Then, different concentrations of CEA were electrochemically detected with the developed NPG/AuE sensing platform. The increasing CEA concentration results in the obvious increase of the response current (Fig. 5C). A good linear relationship between the response current and the CEA concentration is observed in the range of 1 fM to 10 pM CEA, with a fitted equation of I_p (μA) = 0.0342 log(c_{CEA} (M)) + 0.5722 and a correlation coefficient of 0.970 (Fig. 5D). The detection limit is determined to be 0.28 fM CEA, which is comparable with previous reports.[41–44]

Compared with other reported universal electrochemical biosensors (Table S3†), the proposed strategy is able to analyze a wide variety of targets, with a wide linear range and short analysis time, and exhibits advantage in the detection of proteins. With the addition of straightforward operation and low cost, this strategy provides a promising approach for the detection of multiple biomarkers.

To further evaluate the performance of the developed NPG/AuE sensing platform, AuE was used as a substitute to detect Exo III, csDNA, miRNA-21, and CEA, respectively. As shown in Fig. S10,† the obtained response currents are very small, and

there is no obvious linear relationship between the current responses and the target concentrations, which might be ascribed to the fact that the AuE cannot enrich plentiful enough MB-labelled DNA due to limited specific surface area and the non-specific adsorption of macromolecular proteins such as nucleases which block the active site for the cleaved DNA residues with a MB label. In contrast, the bicontinuous porous structure of NPG provides large specific surface area for the enrichment of short DNA residues with a MB label, while blocking the diffusion of macromolecules towards the inner structure of NPG, which is critical for the development of this novel and unique universal electrochemical sensing strategy.

Sound specificity and anti-interference capability are the precondition of reliable universal detection. Therefore, additional experiments were conducted to verify the related properties of the proposed sensing strategy. Among csDNA, miRNA-21, and CEA, once the intended target molecule was selected, the other two served as the interferents, and the corresponding DNA recognizer and nuclease that were matched with the intended target molecule were used for the test. To expand test coverage, single-base mismatched csDNA (csDNA-1), miRNA-141, and alpha-fetoprotein (AFP) were selected as additional common interferents. As depicted in Fig. S11,† compared with the significant response current towards the intended target, the current signal for each interferent is negligible. And then, the mixture of the intended target and all the interferents was detected. As a result, a response current almost equal to that for the intended target alone was obtained, demonstrating the high specificity and anti-interference capability of the proposed sensing strategy. Such a high specificity is achieved through triple specific recognitions, including recognition of specific target by corresponding DNA recognizers, specific cleavage based on nucleases, and specific screening and enrichment of short MB-tagged DNA residues by NPG/AuE sensing platform.

Complex sample analysis

Firstly, the applicability of the developed NPG/AuE sensing platform in the analysis of complex biological systems was investigated through spike/recovery experiments, where different concentrations of csDNA were added into 10-fold diluted healthy human serum and detected by the assay illustrated in Fig. 3A. As presented in Table S4,† good recoveries ranging from 98.4 to 101.6 are obtained with the relative standard deviations (RSDs) of less than 1.64%, suggesting that the developed NPG/AuE sensing platform has superior anti-interference ability in complex system analysis and holds great potential in the clinical sample analysis applications for various purposes. To more comprehensively study the analytical performance of the NPG/AuE sensing platform in complex biological system, the calibration plots for csDNA, miRNA-21, and CEA spiked serum samples were established respectively (Fig. S12–S14†). The fitted linear regression equations for csDNA, miRNA-21, and CEA calibration plots are I_p (μA) = 0.0894 log(c_{csDNA} (M)) + 1.6246, I_p (μA) = 0.0137 log($c_{miRNA\text{-}21}$ (M)) + 0.2017, and I_p (μA) = 0.0323 log(c_{CEA} (M)) + 0.5489, respectively. The detection limits are determined to be 7.42 fM csDNA, 39.20 fM miRNA-21, and 0.40 fM CEA, respectively. Interestingly, compared with the linear equation and the detection limit in standard buffer solution, the analytical performance of the NPG/AuE sensing platform is not influenced significantly by the matrix effects of serum, demonstrating the strong anti-interference capability of the proposed strategy and platform in complex biological samples. This positive result could be attributed to the strong anti-fouling property of the NPG film.

Furthermore, to investigate the practical feasibility of the proposed sensing strategy and platform in real sample analysis, eight clinical serum samples, including four samples from healthy individuals and four samples from breast cancer patients, were collected from Qilu Hospital of Shandong University in accordance with the rules of the local ethical committee. The miRNA-21 level and the CEA level in these samples were determined based on the corresponding calibration plots in spiked serum samples. To validate the reliability of the obtained results, commercial electrochemiluminescence (ECL) and Quantitative Real-time Polymerase Chain Reaction (qRT-PCR) were employed as the standard method for CEA and miRNA-21 analysis, respectively. As exhibited in Fig. 6, the proposed sensing strategy can not only distinguish the positive samples from the negative samples accurately, but also shows good agreement with commercial methods, demonstrating promising application potential in clinical practice.

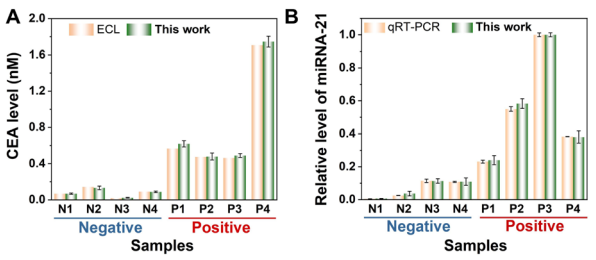

Fig. 6 (A) The CEA levels in real serum samples determined by the proposed strategy and commercial ECL. ECL results are clinical outcomes provided by the hospital. (B) The relative levels of miRNA-21 in real serum samples determined by the proposed strategy and commercial qRT-PCR assay.

Conclusions

In conclusion, the unique nanoporous structure of NPG endows it with an enlarged surface area, excellent electrochemical catalytic activity, and superior mass transfer capability, resulting in at least a 15-fold increase in free MB response compared with the planar AuE. DNA length and configuration have an obvious influence on their transport into the nanostructure of the NPG platform. The NPG/AuE sensing platform can not only distinguish and quantify short DNA strands within a certain range of chain length, but also effectively prevent the diffusion of long DNA with a large configuration, which allows convenient homogeneous assays. Moreover, the relationship between the electrochemical response signal and the length of ssDNA was established, laying a foundation for various analytical applications and background signal reduction. Based on the full understanding of the structure–property relationship between the DNA length/configuration and the corresponding

electrochemical response of the NPG sensing platform, different types of targets, including Exo III, csDNA, miRNA-21, and CEA, were sensitively and specifically detected by combining the NPG/AuE sensing platform with corresponding recognition and amplification strategies, demonstrating the powerful universality of the proposed sensing approach and platform. In addition, the anti-biofouling property of the NPG platform ensures the anti-interference capability and the reliability in real sample analysis, which has been validated by commercial methods, demonstrating promising prospects for application in clinical diagnosis. Moreover, this universal sensing strategy can be easily integrated with multiple electrochemical indicators or multichannel microfluidic devices to achieve simultaneous detection of multiple biomarkers, thereby providing comprehensive biomolecular information for efficient and accurate disease diagnosis and individualized therapy. Therefore, the proposed sensing principle and platform hold great potential in the development of simple, sensitive, comprehensive, and robust point-of-care systems for the healthcare industry.

Data availability

The data supporting this article have been included as part of the ESI.†

Author contributions

Cong-Lin Zhao conducted most experiments, performed the data analysis, and wrote the draft of manuscript. Runlei Gao and Yinzheng Niu conducted some experiments. Bin Cai contributed to supervision and manuscript review & editing. Ye Zhu contributed to supervision, funding acquisition, and manuscript review & editing. All authors reviewed the manuscript and provided valuable feedbacks.

Conflicts of interest

There are no conflicts to declare.

Acknowledgements

This work was supported by Natural Science Foundation of Shandong Province (ZR2020MB059, ZR2023YQ039), Guangdong Basic and Applied Basic Research Foundation (2021A1515220127, 2022A1515012518), National Natural Science Foundation of China (52201262), the Taishan Scholars Program of Shandong Province (tsqn202211042), and the Science and Technology Innovation Committee of Shenzhen Municipality (GJHZ20220913142604008).

Notes and references

1 Y. Y. Xu, Q. Zhang, R. Z. Chen, H. T. Cao, J. Tang, Y. Q. Wu, X. Lu, B. B. Chu, B. Song, H. Y. Wang and Y. He, *J. Am. Chem. Soc.*, 2022, **144**, 23522–23533.
2 T. G. Drummond, M. G. Hill and J. K. Barton, Electrochemical DNA sensors, *Nat. Biotechnol.*, 2003, **21**, 1192–1199.
3 H. X. Yu, O. Alkhamis, J. Canoura, Y. Z. Liu and Y. Xiao, *Angew. Chem., Int. Ed.*, 2021, **60**, 16800–16823.
4 A. Klebes, H. C. Ates, R. D. Verboket, G. A. Urban, F. von Stetten, C. Dincer and S. M. Früh, *Biosens. Bioelectron.*, 2024, **244**, 115800.
5 S. Bracaglia, S. Ranallo and F. Ricci, *Angew. Chem., Int. Ed.*, 2023, **62**, e202216512.
6 E. Vargas, F. Zhang, A. Ben Hassine, V. Ruiz-Valdepeñas Montiel, R. Mundaca-Uribe, P. Nandhakumar, P. T. He, Z. Y. Guo, Z. D. Zhou, R. H. Fang, W. W. Gao, L. F. Zhang and J. Wang, *J. Am. Chem. Soc.*, 2022, **144**, 17700–17708.
7 L. R. Arias-Aranda, G. Salinas, A. Kuhn, G. Xu, F. Kanoufi, L. Bouffier and N. Sojic, *Chem. Sci.*, 2024, **15**, 8723–8730.
8 W. Liu, Q. Zhu, C. N. Yang, Y. H. Fu, J. C. Zhang, M. Y. Li, Z. L. Yang, K. L. Xin, J. Ma, M. Winterhalter, Y. L. Ying and Y. T. Long, *Nat. Nanotechnol.*, 2024, **19**, 1693–1701.
9 J. Das, I. Ivanov, L. Montermini, J. Rak, E. H. Sargent and S. O. Kelley, *Nat. Chem.*, 2015, **7**, 569–575.
10 L. Q. Zhang, S. Wan, Y. Jiang, Y. Y. Wang, T. Fu, Q. L. Liu, Z. J. Cao, L. P. Qiu and W. H. Tan, *J. Am. Chem. Soc.*, 2017, **139**, 2532–2540.
11 S. Somasundaram and C. J. Easley, *J. Am. Chem. Soc.*, 2019, **141**, 11721–11726.
12 V. Ruiz-Valdepenas Montiel, J. R. Sempionatto, B. E.-F. de Avila, A. Whitworth, S. Campuzano, J. M. Pingarron and J. Wang, *J. Am. Chem. Soc.*, 2018, **140**, 14050–14053.
13 Z. Y. Zhou, S. Mukherjee, S. J. Hou, W. J. Li, M. Elsner and R. A. Fischer, *Angew. Chem., Int. Ed.*, 2021, **60**, 20551–20557.
14 M. Gutiérrez-Capitán, A. Sanchís, E. O. Carvalho, A. Baldi, L. Vilaplana, V. F. Cardoso, Á. Calleja, M. Wei, R. de la Rica, J. Hoyo, A. Bassegoda, T. Tzanov, M.-P. Marco, S. Lanceros- Méndez and C. Fernández-Sánchez, *ACS Sens.*, 2023, **8**, 3032–3042.
15 F. Q. Li, W. Q. Yang, B. Zhao, S. Yang, Q. Y. Tang, X. J. Chen, H. L. Dai and P. F. Liu, *Adv. Sci.*, 2022, **9**, 2102804.
16 S. M. Imani, E. Osman, F. Bakhshandeh, S. Qian, S. Sakib, M. MacDonald, M. Gaskin, I. Zhitomirsky, D. Yamamura, Y. Li, T. F. Didar and L. Soleymani, *Adv. Sci.*, 2023, **10**, 2207223.
17 J. J. Qin, W. Wang, L. Q. Gao and S. Q. Yao, *Chem. Sci.*, 2022, **13**, 2857–2876.
18 L. L. Zhang, C. B. Zhong, T. J. Huang, L. M. Zhang, F. Yan and Y. L. Ying, *Chem. Sci.*, 2024, **15**, 8355–8362.
19 Z. Y. Liu, X. H. Shan, Q. Xue, Y. Liu, L. He and H. J. Xie, *Chem. Eng. J.*, 2023, **473**, 145486.
20 M. S. Yao, W. X. Tang, G. E. Wang, B. Nath and G. Xu, *Adv. Mater.*, 2016, **28**, 5229–5234.
21 E. Gonzalez-Martinez, S. Saem, N. E. Beganovic and J. M. Moran-Mirabal, *Angew. Chem., Int. Ed.*, 2023, **62**, e202218080.
22 H. Kwon, H.-N. Barad, A. R. S. Olaya, M. Alarcón-Correa, K. Hahn, G. Richter, G. Wittstock and P. Fischer, *ACS Catal.*, 2023, **13**, 11656–11665.

23 G. Wittstock, M. Bäumer, W. Dononelli, T. Klüner, L. Lührs, C. Mahr, L. V. Moskaleva, M. Oezaslan, T. Risse, A. Rosenauer, A. Staubitz, J. Weissmüller and A. Wittstock, *Chem. Rev.*, 2023, **123**, 6716–6792.
24 J. Yoon, B. M. Conley, M. Shin, J.-H. Choi, C. K. Bektas, J.-W. Choi and K.-B. Lee, *ACS Nano*, 2022, **16**, 5764–5777.
25 Z. J. Zhang, P. Sen, B. R. Adhikari, Y. F. Li and L. Soleymani, *Angew. Chem., Int. Ed.*, 2022, **61**, e202212496.
26 P. Sen, Z. Zhang, S. Sakib, J. Gu, W. Li, B. R. Adhikari, A. Motsenyat, J. L'Heureux-Hache, J. C. Ang, G. Panesar, B. J. Salena, D. Yamamura, M. S. Miller, Y. F. Li and L. Soleymani, *Angew. Chem., Int. Ed.*, 2024, **63**, e202400413.
27 J. Q. Deng, C. Liu and J. S. Sun, *Adv. Mater.*, 2023, **36**, 2303092.
28 S. Jaitpal, K. W. Ng, A. M. S. Juan, C. Martinez, C. Phillips, S. Tripathy and S. Mabbott, *Chem. Sci.*, 2024, **15**, 8112–8126.
29 P. Daggumati, S. Appelt, Z. Matharu, M. L. Marco and E. Seker, *J. Am. Chem. Soc.*, 2016, **138**, 7711–7717.
30 Z. Matharu, P. Daggumati, L. Wang, T. S. Dorofeeva, Z. Li and E. Seker, *ACS Appl. Mater. Interfaces*, 2017, **9**, 12959–12966.
31 Y. H. Tan, J. A. Davis, K. Fujikawa, N. V. Ganesh, A. V. Demchenko and K. J. Stine, *J. Mater. Chem.*, 2012, **22**, 6733–6745.
32 Y. Zhu, C. Q. Zhou, X. P. Yan, Y. Yan and Q. Wang, *Anal. Chim. Acta*, 2015, **883**, 81–89.
33 H. Han, J. H. Jeung, S. H. Jang, C. Y. Lee and J. K. Ahn, *Int. J. Mol. Sci.*, 2023, **24**, 12330.
34 X. Zhang, Y. Bai, Y. J. Jiang, N. Wang, F. F. Yang, L. Zhan and C. Z. Huang, *Anal. Methods*, 2021, **13**, 1489–1494.
35 X. D. Liu, T. Bing and D. H. Shangguan, *ACS Appl. Mater. Interfaces*, 2017, **9**, 9462–9469.
36 S. T. Shanmugam, S. Trashin and K. De Wael, *Biosens. Bioelectron.*, 2022, **195**, 113652.
37 Y. M. Zhou, S. P. Xie, B. Liu, C. Wang, Y. B. Huang, X. R. Zhang and S. S. Zhang, *Anal. Chem.*, 2023, **95**, 3332–3339.
38 X. F. Liu, Q. Wang, Y. Zhang, Z. H. Yang, N. Li, Y. Xu, M. Yang, D. Q. Huo and C. J. Hou, *Chem. Eng. J.*, 2024, **479**, 147231.
39 W. Wang, L. Liu, J. X. Zhu, Y. Q. Xing, S. L. Jiao and Z. Wu, *ACS Nano*, 2024, **18**, 6266–6275.
40 H. Zhang, Y. Tang, Y. S. Zhou, Y. G. Wang, H. B. Si, L. Li and B. Tang, *Chem. Sci.*, 2024, **15**, 9345–9352.
41 M. D. Gholami, S. Nihal, Q. Liu, D. Sarfo, P. Sonar and E. L. Izake, *Sens. Actuators, B*, 2023, **393**, 134208.
42 Q. Niu, L. L. Fu, Y. X. Zhong, B. Cui, G. L. Zhang and Y. P. Yang, *Anal. Chem.*, 2022, **95**, 1123–1131.
43 S. G. Meirinho, L. G. Dias, A. M. Peres and L. R. Rodrigues, *Biotechnol. Adv.*, 2016, **34**, 941–953.
44 Y. T. Shi, T. T. Li, L. Zhao, Y. J. Liu, K. X. Ding, D. X. Li, P. He, D. G. Jiang, J. Liu and H. Zhou, *Biosens. Bioelectron.*, 2023, **230**, 115287.